JOURNAL OF GEOPHYSICAL RESEARCH: ATMOSPHERES, VOL. 118, 1–13, doi:10.1002/2013JD020908, 2013

Dynamic variability of the Asian monsoon anticyclone observed in potential vorticity and correlations with tracer distributions

H. Garny[1] and W. J. Randel[2]

Received 18 September 2013; revised 3 December 2013; accepted 3 December 2013.

[1] The Asian summer monsoon is associated with strong upward transport of tropospheric source gases and isolation of air within the upper tropospheric anticyclone, with a high degree of dynamical variability. Here we study the anticyclone in terms of potential vorticity (PV) as derived from reanalysis data. The strength of the anticyclone, as measured by low PV area, varies on subseasonal time scales (periods of 30–40 days), driven by variability in convection. The convective forcing of low PV areas is associated with heating in the middle troposphere and divergent motion in the upper troposphere, and we find that upper level divergence is a good predictor of the anticyclone strength. Low PV air is often observed to propagate from the forcing region to the west, and occasionally to the east. Carbon monoxide (CO) measured by the Aura Microwave Limb Sounder is used to study the covariability of chemical tracers with the anticyclone strength and location. Concentrations of CO maximize within the upper tropospheric anticyclone, and enhanced CO is well correlated with the spatial distribution of low PV. Time variations of CO concentrations in the upper troposphere (around 360 K) are not strongly correlated with anticyclone strength, probably because CO transport also involves coupling with surface CO sources (unlike PV). Temporal correlations with PV are stronger for CO at higher levels (380–400 K), suggesting that advective upward transport is important for tracer evolution at these levels.

Citation: Garny, H., and W. J. Randel (2013), Dynamic variability of the Asian monsoon anticyclone observed in potential vorticity and correlations with tracer distributions, *J. Geophys. Res. Atmos.*, *118*, doi:10.1002/2013JD020908.

1. Introduction

[2] In response to persistent convection associated with the Asian summer monsoon, a large-scale anticyclone occurs in the upper troposphere and lower stratosphere (UTLS). The strong circulation of the anticyclone acts to isolate air, and because this isolated air is tied to the outflow of deep convection, the anticyclone often has a distinct chemical signature [*Dethof et al.*, 1999; *Randel and Park*, 2006; *Park et al.*, 2007, 2008; *Baker et al.*, 2011]. The UTLS anticyclone is a seasonal feature, beginning in June and ending in September. The evolution over the season is characterized by large variability in the extent, strength, and location of the anticyclone [*Randel and Park*, 2006]. Oscillations with periods of 10–20 and 30–60 days were found by *Annamalai and Slingo* [2001], and they concluded that these are driven by variations in the monsoon convection. *Zhang et al.* [2002] found that the location of the center of the anticyclone at 100 hPa is bimodal and classified a Tibetan Mode and Iranian Mode according to the location of the center. Associated with these modes, *Yan et al.* [2011] found tracer anomalies that are shifted in longitude depending on the location of the anticyclone. Less detail is known of subseasonal variations in tracers and their links with dynamical variability of the anticyclone on smaller spatial scales.

[3] Linear models closely reproduce the climatological features of the anticyclone as wave response to diabatic heating [*Gill*, 1980; *Hoskins and Rodwell*, 1995]. However, as pointed out by *Plumb* [2007], these linear theories are not consistent with the simple balances of uniform angular momentum in the Hadley cell, and eddy transports and instability are fundamental aspects of the upper troposphere vorticity balance (see also *Sardeshmukh and Held* [1984]). *Hsu and Plumb* [2000] show with an idealized nonlinear model that the response to divergent flow under conditions representative of the real atmosphere becomes unstable, and eddy transport of potential vorticity (PV) by "eddy shedding" from the anticyclone occurs. *Hsu and Plumb* [2000] and *Popovic and Plumb* [2001] show evidence of eddy shedding from observations. Figure 1 shows an example of the dynamic variability of the anticyclone over 9–19 June 2006 viewed in terms of potential vorticity (PV). The anticyclone is a region of low PV, and this sequence highlights fine-scale structure and propagation of low PV air both to the east and to the west of the anticyclone center, coincident with weakening of the anticyclone. In particular, the

[1]Deutsches Zentrum für Luft- und Raumfahrt, Institut für Physik der Atmosphäre, Oberpfaffenhofen, Germany.
[2]National Center for Atmospheric Research, Boulder, Colorado, USA.

Corresponding author: H. Garny, Deutsches Zentrum für Luft- und Raumfahrt, Institut für Physik der Atmosphäre, DE-82234 Oberpfaffenhofen, Germany. (hella.garny@dlr.de)

2169-897X/13/10.1002/2013JD020908

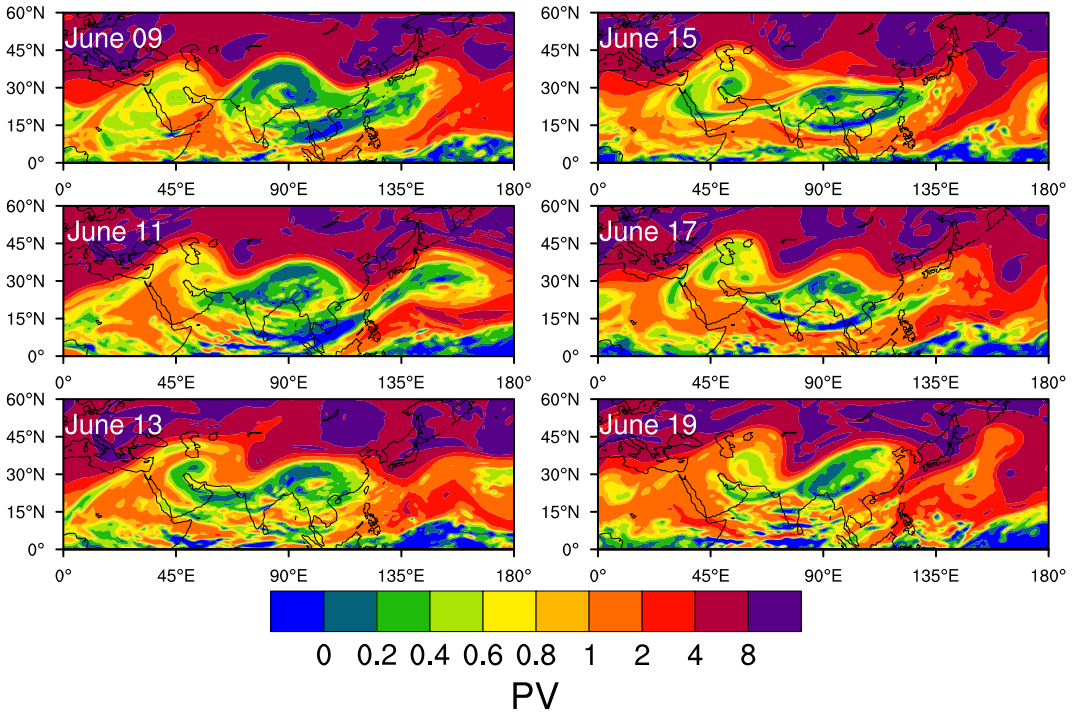

Figure 1. Daily maps of PV in PV units (1 PVU = 10^{-6} K m^2 kg^{-1} s^{-1}) on the 360 K level between 9 and 19 June of the year 2006.

observed sequence of westward propagation is similar to the theoretical model calculation by *Hsu and Plumb* [2000], suggesting that the eddy shedding is an important aspect of anticyclone variability.

[4] The behavior of the anticyclone as a large-scale PV anomaly linked to enhanced tracer gradients is reminiscent of the stratospheric polar vortices [e.g., *Butchart and Remsberg*, 1986; *Nash et al.*, 1996; *Manney et al.*, 2009; *Santee et al.*, 2011]. A useful diagnostic to study the development and confinement of the polar vortices is provided by the time variations of the area enclosed by specific PV isolines. The area of PV is conserved in adiabatic, nondivergent flows, and thus, changes in the area arise from either diabatic processes or divergence. In reality, additional changes in PV area result from mixing into unresolved scales, which occurs in regions of strong stirring, as for example due to wave breaking at the polar vortex edge [*Butchart and Remsberg*, 1986]. The remapping of tracer fields according to their PV value (often referred to as "equivalent latitude") is widely used in studies of the polar stratosphere [e.g., *Bodeker et al.*, 2001; *Waugh and Rong*, 2002] and has the advantage of a more physical separation of air according to its dynamical origin (i.e., inside or outside the vortex) rather than to its geographic location.

[5] In this study, we examine whether PV diagnostics can provide improved understanding of circulation and transport within the monsoon anticyclone. The dynamical drivers of the anticyclone and the polar vortices are quite different: The anticyclone is tied to convective heating and divergent flow located in the tropics, while the cyclonic polar vortices are primarily radiatively driven high-latitude features. However, the confinement of air within the polar vortex is similar to behavior observed in the anticyclone. Part of the motivation of this work is to contrast the behaviors of these two distinct yet similar circulation systems. We also quantify forcing for PV area changes in the anticyclone, in particular, the role of divergence and of transient eddy transport of PV (or "PV mixing"). We further utilize measurements of carbon monoxide (CO) from the Aura Microwave Limb Sounder (MLS) satellite instrument to

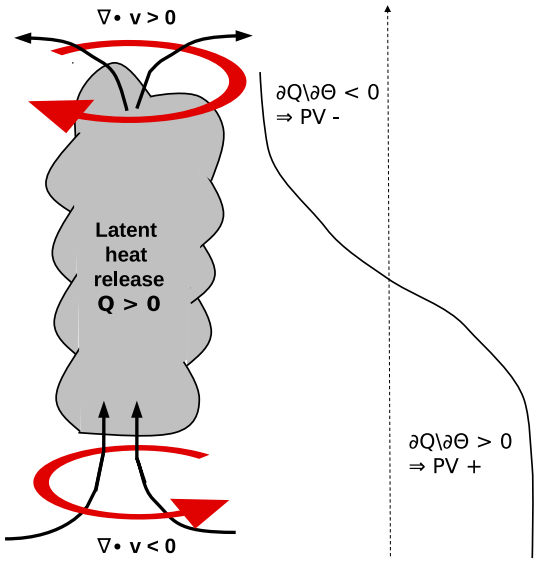

Figure 2. Schematic of the effects of diabatic heating by convection and divergence on PV. On the right, an idealized vertical profile of $\partial Q \backslash \partial \Theta$ is shown.

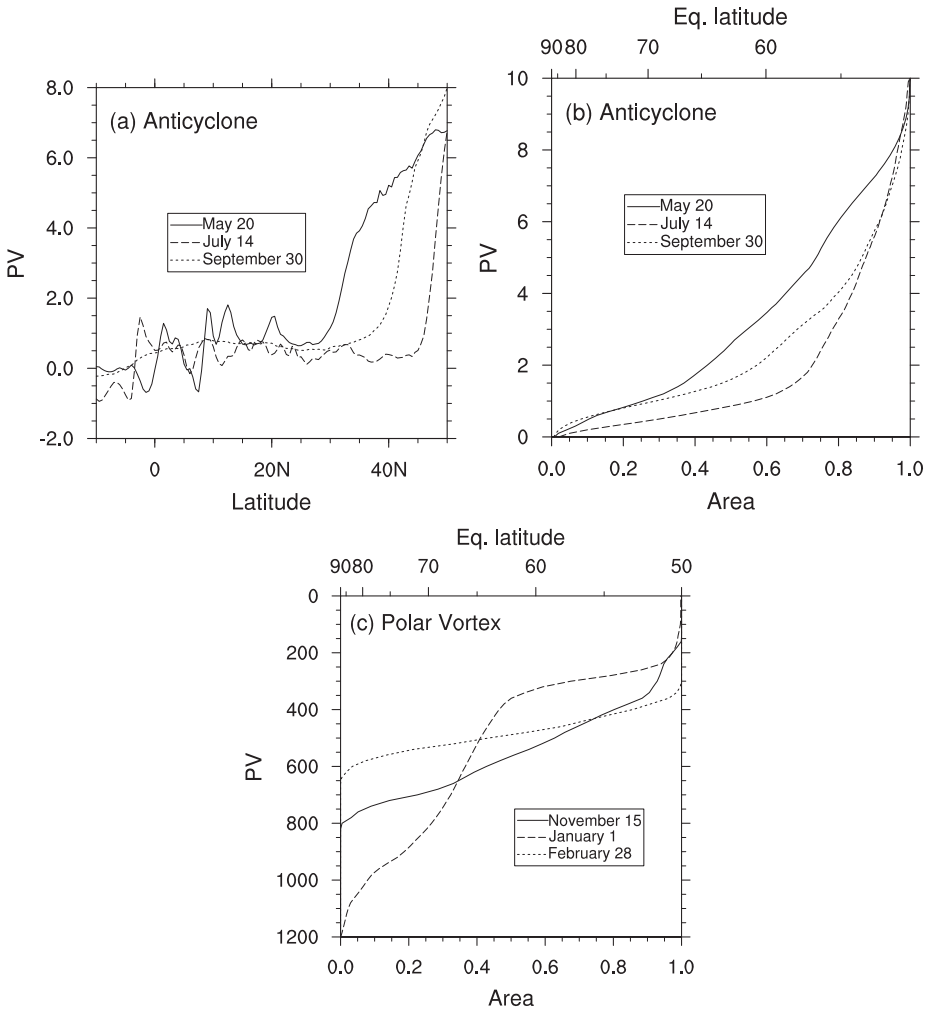

Figure 3. (a) PV at 360 K and at 90°E as a function of latitude for 3 days of the year 2006: 20 May (solid), 14 July (dashed), and 30 September (dotted). (b) Same as Figure 3a but PV in area coordinates (or equivalent latitude, with the lowest PV moved to the pole). The area is calculated in the domain 15°N–45°N and 0°E–180°E and is given in relative units (the area of the whole domain is 1.0). (c) Area of PV for the polar vortex at 850 K for 15 November of the year 2005 (solid), 1 January (dashed), and 28 February (dotted) of year 2006. Here, the area is calculated for the Northern Hemisphere poleward of 50°N.

analyze tracer variability within the anticyclone and quantify links with PV.

2. Data

[6] The analyses in this study are based on a combination of reanalysis data for dynamical quantities and satellite data for trace gases. The Modern-Era Retrospective Analysis for Research and Applications (MERRA) reanalysis data [*Rienecker et al.*, 2011] are used here for the years 2005–2009. These data have high horizontal resolution (0.5° latitude by 0.67° longitude), with a 6-hourly temporal resolution. The wind and temperature fields are used to calculate potential vorticity on isentropic surfaces. CO data are obtained from the Aura Microwave Limb Sounder (MLS) instrument. MLS has been in operation since August 2004. Here, the Level 2 data of version 3.3 are used [*Livesey et al.*, 2011]. The vertical resolution of CO in the upper troposphere and lower stratosphere is about 4.5 km (5 km for temperature). Retrievals of CO are centered on pressure levels of 215, 147, 100, and 68 hPa. The precision of CO data is given with 19, 15, and 14 ppb at 215, 147, and 100 hPa, respectively, and a systematic uncertainty of 30% and 30 ppb is given by *Livesey et al.* [2011]. The screening of the data was performed as suggested in *Livesey et al.* [2011], including scanning for ice water content. For most of the analysis performed in this study, the CO data are used on the satellite track, i.e., directly using values as retrieved from the satellite measurements. For maps of CO, daily gridded fields were constructed with a horizontal resolution of 5° latitude and 10° longitude. We interpolate the CO data from pressure levels to potential temperature levels using the temperatures retrieved from MLS; these interpolated values still represent an average over a broad layer rather than specific levels.

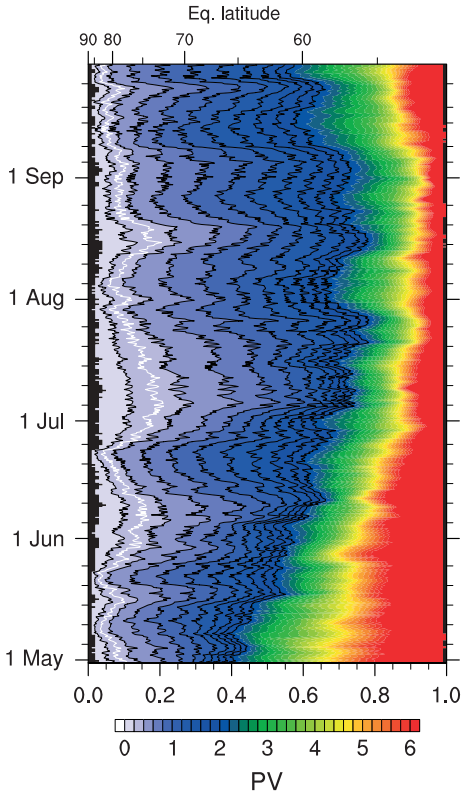

Figure 4. PV at 360 K as function of area (calculated as in Figure 3) contoured for the season from May to September 2006. PV isolines are drawn every 0.2 PVU; contours smaller than 2 PVU are drawn as black lines and the 0.3 PVU isoline in white.

[7] In addition, outgoing longwave radiation (OLR) data are used here as a proxy for deep convection. We use the daily gridded OLR data set from NOAA-CIRES (at http://www.esrl.noaa.gov/psd/data/), which makes use of spatial and temporal interpolation to obtain daily data with a 2.5° latitude and 2.5° longitude resolution. The OLR product is described in *Liebmann and Smith* [1996].

3. Theoretical Background

[8] In this study we use PV to diagnose the location, area, and strength of the anticyclone. Ertel's potential vorticity in isentropic coordinates is defined as

$$\mathrm{PV} = (\xi + f)/\sigma \tag{1}$$

where ξ is the relative vorticity and σ is the isentropic density ($\sigma = -g^{-1}\partial p/\partial\Theta$). PV is a conserved quantity under adiabatic frictionless motion. However, diabatic heating can modify the PV, and the PV equation in isentropic coordinates can be written as follows:

$$\frac{\partial \mathrm{PV}}{\partial t} + v\nabla\mathrm{PV} = \mathrm{PV}\frac{\partial Q}{\partial\Theta} - Q\frac{\partial \mathrm{PV}}{\partial\Theta} \tag{2}$$

where $Q = \partial\Theta/\partial t$ and frictional effects and the tilting term are neglected [*Holton*, 2004].

[9] Following *Butchart and Remsberg* [1986], changes in the PV area $A(t)$ on isentropic levels are given by

$$\frac{\mathrm{d}}{\mathrm{d}t}A(t)_{\mathrm{PV}\le\mathrm{PV}_0} = \underbrace{\oint_\Gamma \left(-\mathrm{PV}\frac{\partial Q}{\partial\Theta} + Q\frac{\partial \mathrm{PV}}{\partial\Theta}\right) dS}_{\text{Diabatic term}} + \underbrace{\int_{A(t)} \nabla\cdot\hat{v}\,\mathrm{d}A}_{\text{Divergence term}} + \underbrace{\oint_\Gamma v\cdot\nabla\mathrm{PV}'\,dS}_{\text{Mixing term}} \tag{3}$$

The circular integral is performed along the edge Γ of the area A, where dS is normalized by the isentropic PV gradient. Variables are divided into an observed part $\hat{x}$ and unresolved part x'. The three terms on the right-hand side represent (1) diabatic heating or cross-isentropic transport, (2) divergent motion which expands the low PV area, and (3) mixing of air to unresolved scales.

[10] Links between deep convection and variations of PV in the upper troposphere are highlighted in Figure 2. The vertical gradient of convective heating (Q) leads to the "generation" of low PV in the upper troposphere, and the vertical advection of PV by Q also reduces PV at higher levels, as PV increases with height (diabatic term in equation (3)). Note that the vertical PV gradient may be influenced by PV variations in the inflow region of the monsoon. Upper level divergence associated with convective outflow leads to an expansion of the area of low PV (divergence term in equation (3)). Note that we put PV "generation" in quotation marks, as low PV cannot be generated but rather the air can be thought of as being diluted and therewith PV is reduced (following the discussion in *Haynes and McIntyre* [1987]). The third term in equation (3) is associated with mixing to unresolved scales and cannot be explicitly calculated in observational data.

[11] Because of the complex nature of the PV budget (especially applied to reanalysis data sets), we have diagnosed balances in a free-running general circulation model (GCM) (Appendix A). The key result there is that the divergence term in equation (3) is a useful single proxy for diagnosing PV area changes: both the diabatic and divergence term in equation (3) represent effects of convection, and the two terms are well correlated, so that the divergence can be utilized as a proxy for convective forcing of low PV areas.

4. PV Variability and Budget for the Anticyclone

[12] We focus analyses on PV fields on the 360 K level (approximately 150 hPa). We choose this level since the maxima in the wind jets forming the anticyclone occur near 360 K, and thus, the anticyclone is strongest and PV anomalies are largest compared to levels above and below.

4.1. Variability in the Anticyclone Measured by Low PV Area

[13] The latitudinal structure of the anticyclone as seen in PV is illustrated in Figure 3a, showing transects through 90°E (near the center) for individual days during the seasonal evolution: one before the onset of the anticyclone (in May), one during a strong phase (in July), and one during the decaying phase (end of September). The anticyclone is linked to an expansion of low PV over 20°N–40°N,

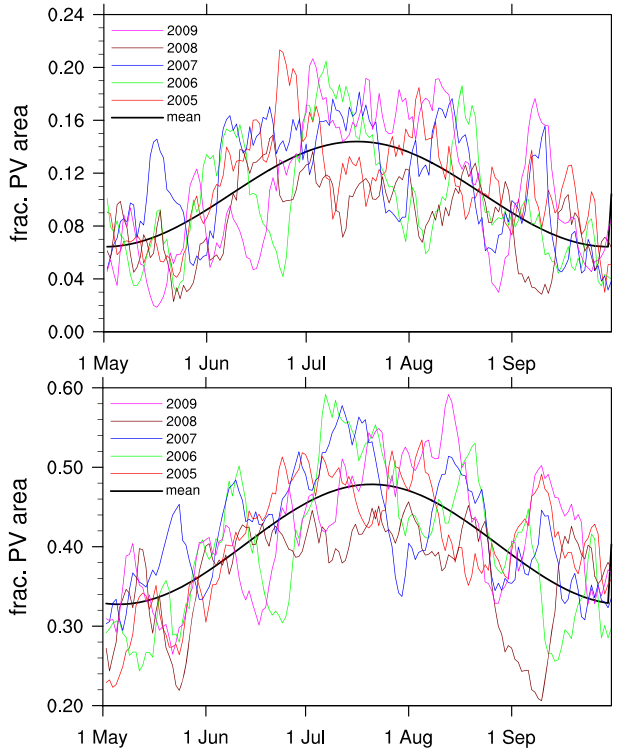

Figure 5. Daily mean PV area at 360 K for (top) PV <= 0.3 PVU and (bottom) PV <= 1 PVU for each year 2005 to 2009 (in colors) and the low-pass filtered 5 year mean with periods shorter than 80 days removed (thick black line).

with strong PV gradients at higher latitudes (marking the transition to the extratropical lower stratosphere) and weak gradients at low latitudes. The weaker PV gradient toward lower latitudes can be expected as PV decreases toward the equator. Daily profiles show a large variability in the PV structure, as is also seen from the daily maps in Figure 1.

[14] The area of low PV contours provides a complementary measure of anticyclone strength. Choosing a domain for the area calculations is a nontrivial issue, as the region should encompass low PV air linked to the anticyclone but not background low PV air from regions close to the equator. We make the subjective choice of 15°N as equatorward boundary, use 45°N as poleward boundary and longitudes of 0°E–180°E. The results shown below change slightly when using 5°N or 10°N instead of 15°N as a lower latitude boundary, but the overall conclusions are not sensitive to the exact choice of the domain. Figure 3b shows the PV area as a function of PV value ($A(\mathrm{PV} \leq \mathrm{PV}_0)$) for the same 3 days as in Figure 3a. In May, only 25% of the area is covered by air with PV $\leq$ 1.0 potential vorticity unit (PVU), and an intermediate gradient to high PV values is found. For the well-established anticyclone in July, the area of low PV expands (PV $\leq$1.0 PVU covering close to 60%), and at the same time the gradient to high (extratropical) PV values is strengthened.

[15] For comparison, the PV area evolution of the Arctic polar vortex during 1 year is illustrated in Figure 3c, showing the formation of a strong vortex between mid-November 2005 and early January 2006, and the decay of the vortex until late February 2006. The area diagnostics for both the anticyclone (Figure 3b) and polar vortex (Figure 3c) are shown as a function of equivalent latitude (upper scales) by remapping the respective regions centered at the pole. These results show that the anticyclone is similar in size to the polar vortex, although its structure in PV is very different. The polar vortex is characterized by high PV values near the center and strong PV gradients at its edge, with weaker gradients outside the vortex indicating the well-mixed "surf zone." In contrast, PV gradients within the anticyclone are relatively weak, suggesting that air is well mixed. Strong PV gradients occur on the poleward (but not equatorward) flank; a sharp PV edge occurs at higher latitudes but a weak and often diffuse separation toward the tropics (which is at least partly a result of the PV decreasing toward the equator). The overall weak PV contrasts and gradients associated with the anticyclone are distinctly different from the polar vortex structure.

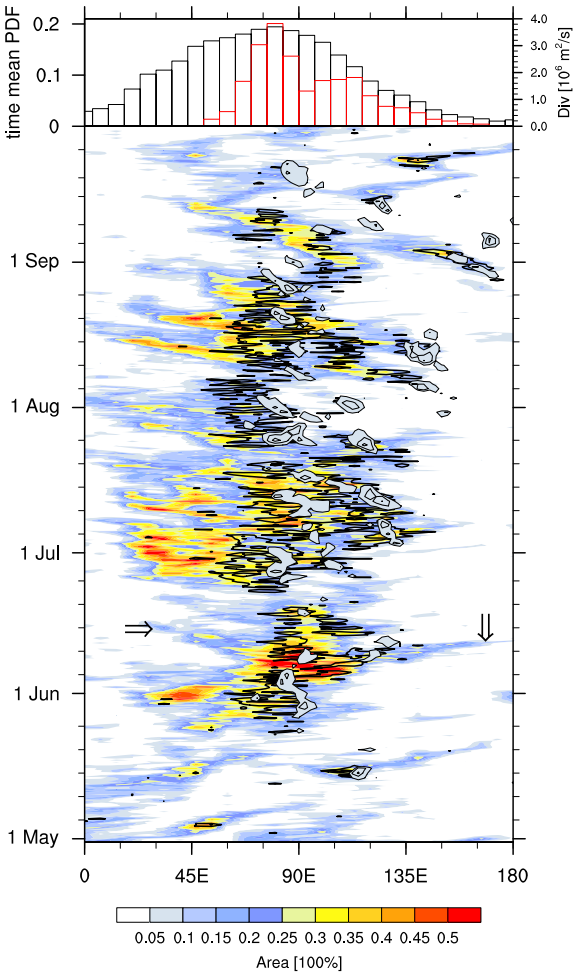

Figure 6. Color contours indicate the area with PV $\leq$0.3 PVU calculated at each longitude for the latitude range 15°N–45°N, spanning May through September 2006. Overlaid are contours of the integrated divergence over the low PV region (in black; contours at 5e6 and 10e6 m^2/s) and contours of averaged OLR over 15°N–30°N (filled in gray, at 190 and 180 W/m^2). The arrows indicate the events from Figure 1. (top) The time mean of the low PV area (black) and the divergence (red).

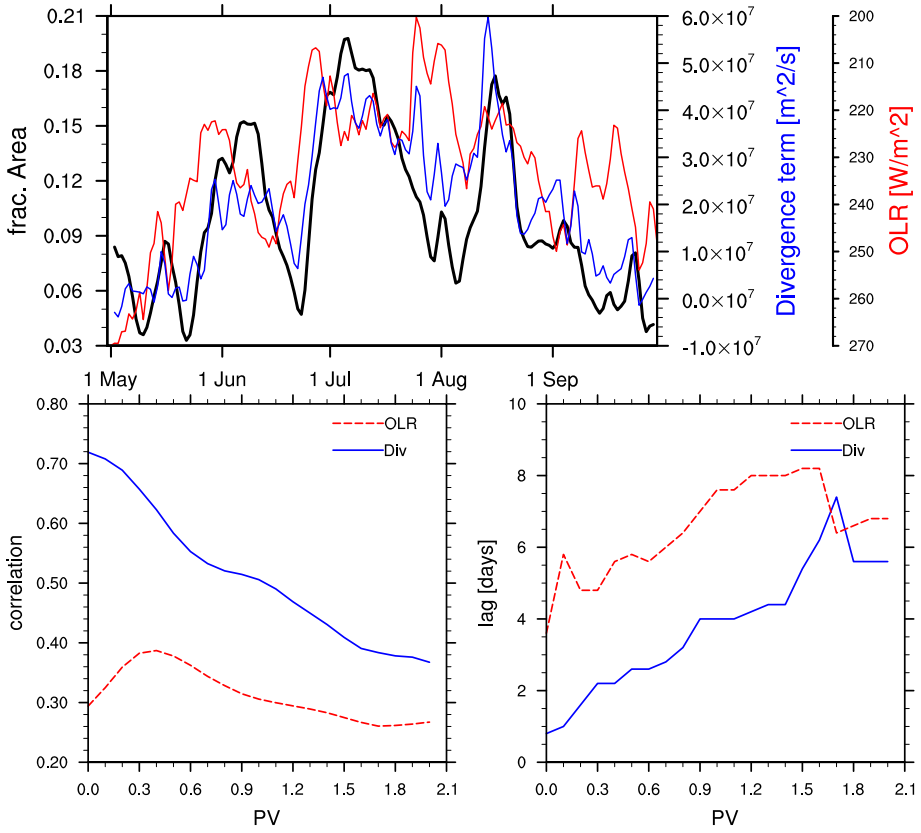

Figure 7. (top) Time series from the year 2006 of daily mean low PV area with PV ≤0.3 PVU (black) together with integrated divergence over this area (blue) and mean OLR over 15°N–30°N and 60°E–120°E (red). (bottom) The 5 year mean (2005–2009) correlation (left) and optimal lag (right) of PV area with divergence (blue) and OLR (red) as a function of PV threshold. The correlations are calculated for each year over the deseasonalized time series from May to September.

[16] The seasonal evolution of the PV area in the anticyclone region for the year 2006 is shown in Figure 4. The area of low PV expands from May to about mid-July and retreats afterward, and subseasonal variations in the strength of the anticyclone are superimposed on the seasonal changes. This seasonal behavior is found as well in other years, as shown in Figure 5 for five different years (2005–2009). The mean seasonal evolution (black line) shows the expansion of low PV in June and decay in late August and September. The seasonal mean evolution is calculated by applying a low-pass filter to the 5 year mean time series, removing periods smaller than 80 days. This seasonal mean evolution is subtracted from time series when calculating correlations and power spectra in the following (referred to as deseasonalized time series). Each year, the low PV areas exhibit strong intraseasonal variability, and this variability is stronger for areas of lower PV thresholds. The variability of the lowest PV isolines are a measure of the intensity of the circulation, and in the following we use the 0.3 PVU area to define the strength of the anticyclone. Variations in higher PV thresholds are correlated with the 0.3 PVU area and lagged slightly in time (1–3 days).

[17] The longitude-time variability of low PV air can be depicted in a Hovmoller diagram, showing the area of low PV (≤0.3 PVU) as a function of longitude and time (Figure 6). Low PV air is most often observed over

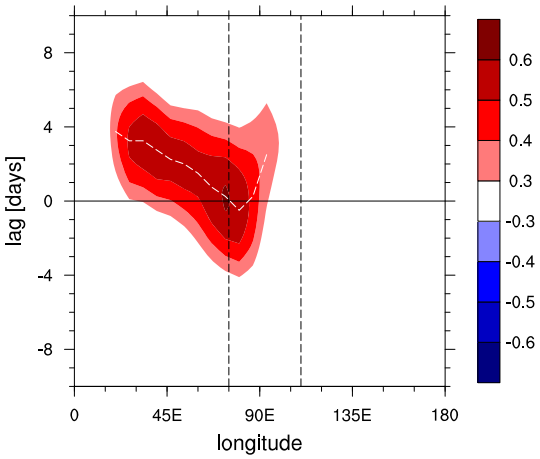

Figure 8. Correlation of low PV area (PV ≤0.3 PVU) at each longitude with respect to the divergence term averaged over 70°E–110°E (indicated by the vertical dashed lines), calculated from data averaged over 2005–2009. The correlations are calculated for each year over the deseasonalized time series from May to September, with periods shorter than 10 days removed from the time series. The dashed white lines give the timing of the maximum correlation at each longitude.

longitudes 75°E–90°E, which we define as the center of the anticyclone. Low PV air is often observed to propagate from the center to the west in Figure 6 and occasionally to the east. For example, the breaking event to the east that was seen in Figure 1 (9–11 June) is apparent as a stretch of low PV toward the east in early/middle June (indicated by the arrow on the right). Likewise, the westward "rolling up" of PV isolines in the following days (13–17 June) is observed as propagation of low PV area toward the west in mid-June (see arrow on left in Figure 6). As seen in Figure 1 the low PV patch is eventually readvected toward the east, being captured in the westerly winds in the northern part of the anticyclone. This behavior is captured only weakly in the Hovmoeller diagram: since the air is mixed with its surrounding in the process, the low PV values are mixed toward higher values which are not detected in the low PV area diagnostic.

4.2. Drivers of Variability in Low PV Area

[18] What drives the intraseasonal variability in the anticyclone? The anticyclone is the upper tropospheric response to diabatic heating by deep convection, and the intensity of deep convection varies over the season, so that the forcing of the anticyclone is itself highly variable. In addition, the dynamical instability of the anticyclone is predicted to lead to transience and periodic eddy shedding. Therefore, in addition to the variability in the forcing, intrinsic dynamic variability can be expected.

[19] Several previous studies have used area-averaged OLR as proxy for the convective influence on the anticyclone [*Randel and Park*, 2006; *Park et al.*, 2007]. Here, we use the PV area equation (equation (3)) to investigate the physical link between convection and the variability of the anticyclone. As discussed in section 3, both diabatic heating due to convection and the divergence associated with the convective outflow lead to increases in the area of low PV. Calculations based on model simulations (Appendix A) suggest that the divergence and diabatic heating terms are closely related, and for simplicity, we use the divergence term as a representation of the effects of convection on low PV area.

[20] Figure 7 shows the time series of the area of low PV (for the PV = 0.3 isoline) together with the mean OLR and the integrated divergence over the low PV area, the latter representing the forcing of the anticyclone according to equation (3). The low PV area is highly correlated with the divergence term (correlation of 0.76), while correlations with OLR are weaker (0.37). For statistics over the 5 years 2005–2009, the low PV area is matched better by the divergence term (correlation of 0.66) than by OLR (correlation of 0.38), as shown in Figure 7 (bottom). Correlations are calculated from deseasonalized time series (see discussion of Figure 5), in order to focus on the intraseasonal variability. The correlation of low PV area is higher with divergence than with OLR for all PV thresholds used to calculate the PV area, but correlations are best for low PV values. The time lag for optimal correlation also increases for higher values of PV, and this is consistent with mixing low PV toward higher PV following convective events, thereby expanding the area of larger PV thresholds. The correlation of the divergence forcing to the low PV area demonstrates a direct physical link between convective

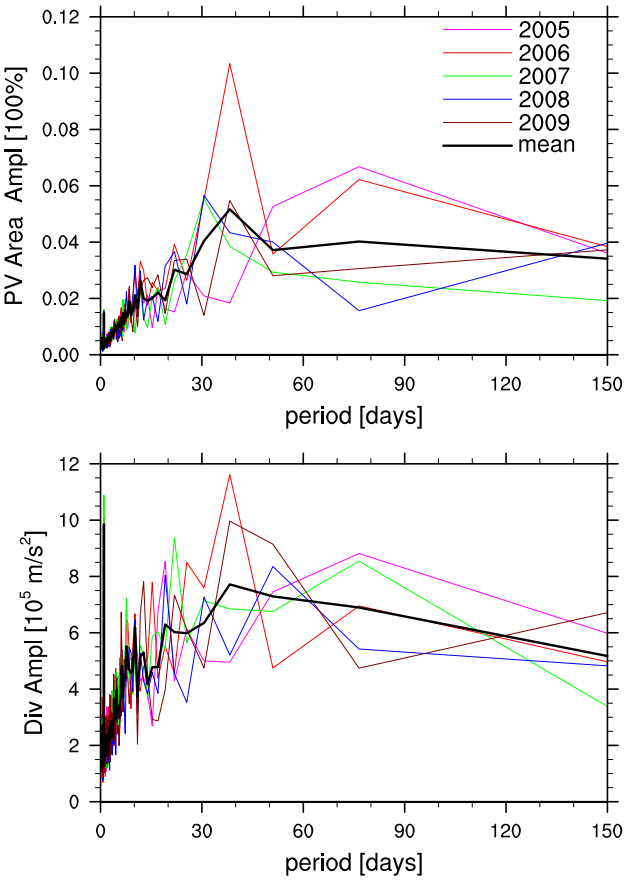

Figure 9. Power spectra of (top) low PV area (PV ≤0.3 PVU) averaged over 70°E–110°E and of the (bottom) divergence term averaged over 70°E–110°E. Spectra are calculated from the deseasonalized May–September time series and are shown for years 2005 to 2009 in color and the averages in black.

forcing and the anticyclone strength. While the correlations with OLR are still statistically significant, our results demonstrate a much stronger and physically meaningful relationship with divergence forcing.

[21] The spatial structure in the forcing of low PV by divergence is also shown in Figure 6. Regions of low PV areas are spatially aligned with strong divergence, in particular, near the center of the anticyclone (between 60°E and 120°E). These longitudes can be identified as the source region of low PV. Enhanced divergence is also linked to the occurrence of deep convection (indicated by contours of low OLR in Figure 6), as expected. To the west of about 60°E, there is little divergence-related low PV "generation," and low PV values in this region are mainly advected from the center of the anticyclone.

[22] The frequent westward propagation of low PV air is reflected in the correlation of PV areas to divergence as a function of longitude as shown in Figure 8: The highest correlation of low PV area to divergence occurs around 80°E–90°E. With increasing time lag, the region of high correlation propagates to the west, and after 4 days the highest correlation is found around 35°E–45°E. At the same time, a weaker signature of eastward propagation of low PV

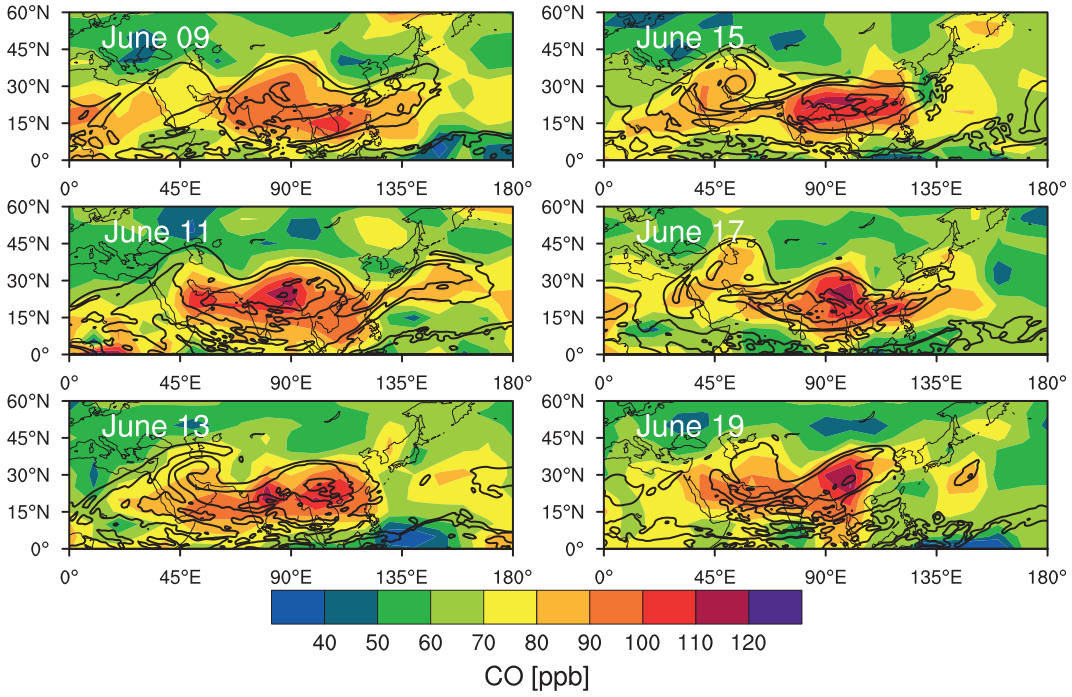

Figure 10. Daily CO maps at 360 K from 9 to 19 June of the year 2006 (colored contours). Superimposed are PV contours of smoothed PV fields at 0.4 and 1 PVU (black).

area from the center is indicated by the eastward shift of maximum correlations at longitudes east of 80°E.

[23] We have furthermore investigated temporal variability of low PV area as reflected via spectrum analysis. The power spectra of the low PV area in the center of the anticyclone reveals a peak in power at 30–40 days and generally decreases at shorter and longer time periods (see Figure 9). The decrease in power at longer periods is due to subtracting the seasonal mean evolution; otherwise, power would increase for periods greater than 80 days. Likewise, variability in divergence calculated in the same manner (Figure 9, bottom) maximizes at periods of 30–40 days. This is consistent with our finding that the main intraseasonal variability in low PV area is driven by variations in the divergence term.

5. Variability in Chemical Tracers

[24] Chemical tracers give a complementary perspective on anticyclone structure and variability [e.g., *Park et al.*, 2009]. Here we investigate this variability (and links to PV) using CO measurements from the MLS instrument. CO is well suited for this purpose as it has mostly tropospheric sources and a photochemical lifetime of 2–3 months, i.e., longer than the typical transport time scales in the monsoon system. We address questions including the following: Do the distortions and eddy shedding from the anticyclone as observed in PV fields impact tracer fields, and how are tracer anomalies observed in the upper troposphere correlated with the strength of the anticyclone? Our analyses focus on relationships with PV at the 360 K level, where correlations are strongest. Links to PV at other levels are discussed below.

[25] Figure 10 shows the sequence of daily maps as in Figure 1 for the gridded CO concentrations from MLS. The highest CO concentrations are found within the low PV contours (i.e., within the anticyclone) and the CO contours follow similar patterns to the PV. For example, along with the eastward movement of low PV air over 9–11 June, a patch of air with high CO concentrations moves to the east. Likewise, the distortion and rolling up of low PV air toward the west on 13–17 June is accompanied with high CO air. However, much of the fine-scale structures that are seen in PV are not observed in the CO fields, possibly due to the coarser resolution of the gridded CO fields compared to the PV fields.

[26] Figure 11 shows a second example of large-scale dynamic variability of the anticyclone that is closely coupled to CO. This event (over 28 August to 1 September 2006) shows a remarkable splitting of the anticyclone into two separate PV minima, accompanied by large-scale CO structure that mirrors the PV. Such spatially coupled behavior between PV and CO is observed throughout the highly dynamic life cycle of the anticyclone each year, although the temporal variations in PV and CO can be distinct (as they have different sources, as discussed below).

[27] Figure 12 (left) shows a Hovmoller diagram illustrating the covariability of high CO concentrations at 360 K with the area of low PV (here the PV is smoothed to match the lower horizontal and temporal resolution of the CO data). These calculations use an area diagnostic for CO by calculating the fraction of the measurement points in the domain that exceed a specified threshold (here 100 ppb). The advantage is that this calculation can be applied directly to the retrieved data on the satellite orbit measurement points (although this area diagnostic applied on the gridded CO data yields similar results). For the 360 K level the threshold value of 100 ppb was chosen as to maximize the correlation of high CO areas to the low PV areas.

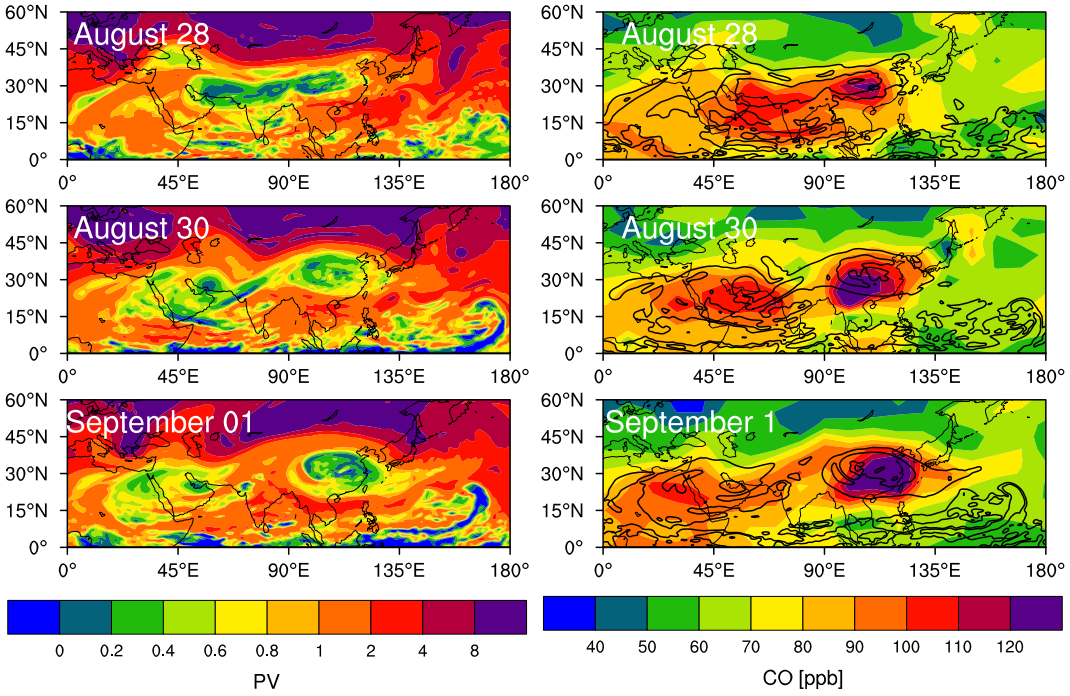

Figure 11. (left) Daily PV and (right) CO maps at 360 K as in Figures 1 and 10 but for 28 August to 1 September.

[28] The regions of frequent occurrence of high CO concentrations in Figure 12 generally overlap with low PV regions (i.e., high CO within the anticyclone), although not all features are reproduced. Several of the westward or eastward propagation events can be observed in both quantities. For example, the strong low PV area in mid-July is colocated with elevated CO concentrations, and both the eastward and westward propagation of low PV is matched by high CO. In other cases the correlation is less evident, such as for the case of 9–17 June (Figure 10). This is partly because the CO

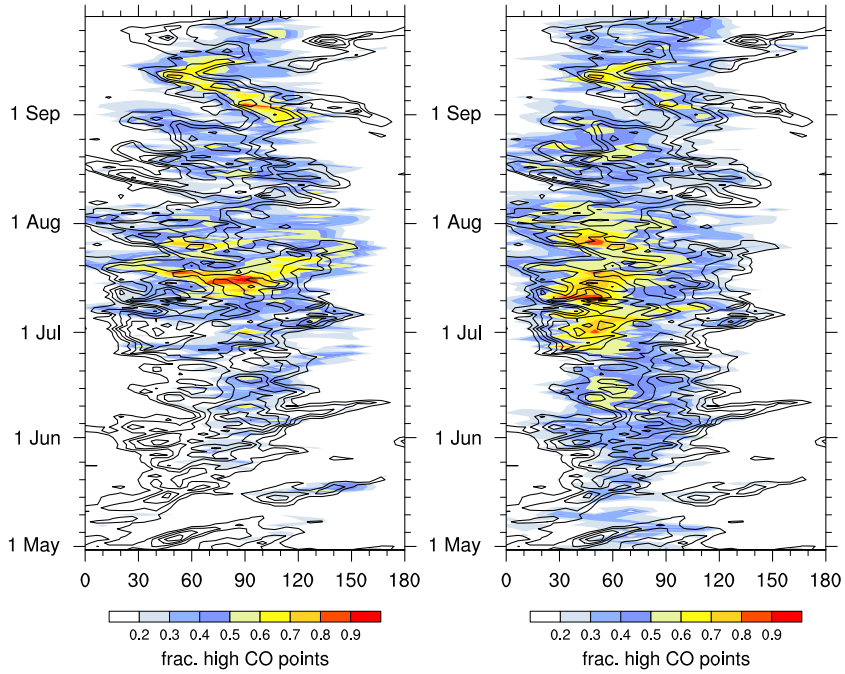

Figure 12. Hovmoeller diagram of the fraction of measurement points where CO concentrations are (left) above 100 ppb at 360 K and (right) above 80 ppb at 380 K at each longitude over 15°N–45°N. Overlaid are contours of low PV area (PV ≤0.3 PVU) as in Figure 6 but using smoothed PV fields to match lower resolution of MLS data (black contours). These data are for the year 2006.

values fall below the threshold of 100 ppb and are not captured by the diagnostic.

[29] The overall correlation between the area of low PV and area of high CO at 360 K seen in Figure 12 is 0.49. The spatial and temporal correlations can be calculated separately, i.e., the spatial (longitudinal) correlation can be calculated for each day and averaged in time, and likewise for the temporal correlation at each longitude. The spatial correlation (0.53) is significantly higher than the temporal correlation (0.30) between low PV area and area of high CO at 360 K. Similar results are derived for the years 2005–2009. Figure 12 (right) shows similar calculations for CO at the 380 K level using a threshold value of 80 ppbv. Here the most frequent enhanced CO values occur to the west of the maxima at 360 K, and there are stronger correlations with PV (overall correlation is 0.63; spatial $r = 0.64$ and temporal $r = 0.37$).

[30] Another way to examine the CO concentrations relative to PV is to calculate the mean CO concentrations along PV contours, which can reveal the degree of alignment of CO anomalies with the PV fields. This is essentially the same as calculating tracer distributions in equivalent latitude as often done for the polar vortices [*Butchart and Remsberg*, 1986]. Figure 13 shows the 360 K CO concentrations in PV area coordinates together with the PV contours (repeated from Figure 4). This calculation shows that the highest CO concentrations occur where PV is lowest (i.e., in the center of the anticyclone). Furthermore, CO concentrations larger than 80 ppbv are confined to regions where the PV is lower than 2 PVU (indicated in Figure 13, white line). In other words, the steepening of PV gradients at the edge of the extratropics (PV >2 PVU) forms a barrier for air with high CO concentrations.

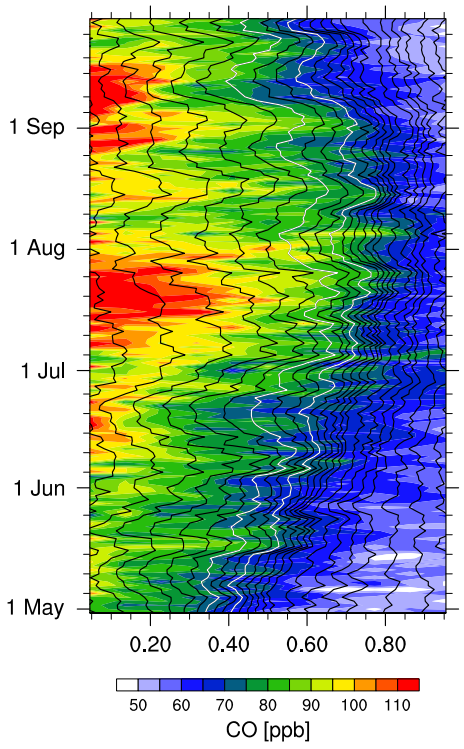

Figure 13. Black contours show time series of PV area as in Figure 4, and colors indicate CO concentrations averaged along PV contours. The 1.4 and 2 PVU contours are marked in white.

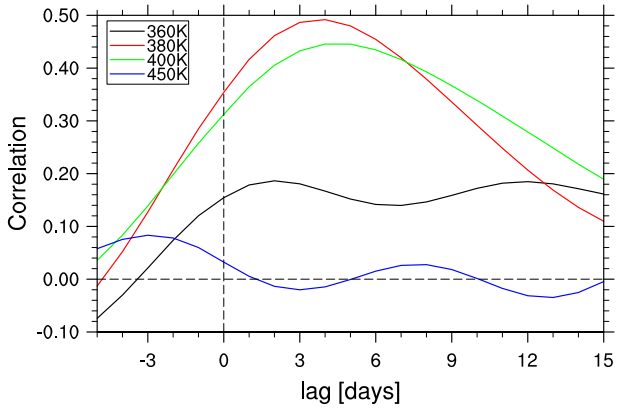

Figure 14. Correlation of the time series of 0.3 PV area at 360 K to the area of high CO concentrations at 360, 380, 400, and 450 K, where the CO thresholds are 100, 80, 65, and 35 ppb, respectively. Correlations are calculated from deseasonalized May–September time series for each year 2005–2009, and the 5 year mean is shown.

[31] The temporal variations in Figure 13 show that there is not a strong correlation between the peaks in CO amounts and variations in the anticyclone strength (area of the low PV contours). For example, the anticyclone strength peaks in early July, while CO concentrations maximize in the latter half of July. The amount of CO at 360 K is presumably related to convective outflow (similar to PV) but also linked to surface sources of CO (unlike PV). The temporal correlation for CO concentrations at 360 K is below 0.2 in the 5 year mean (Figure 14). However, the correlation with anticyclone strength is stronger for CO at higher levels of 380 to 400 K (i.e., around 100 hPa), while it becomes insignificant above (see Figure 14). The strongest correlation is found between the anticyclone strength and enhanced CO concentrations at 380 K with a lag of 4 days. Correlations of low PV areas at 380 K to CO at any of the regarded levels are lower. Overall, PV at 380 K appears to be a poorer diagnostic for the anticyclone strength, for reasons that will be discussed in the next section.

6. Summary and Discussion

[32] The Asian monsoon anticyclone is associated with relatively low values of PV in the UTLS, and this work has focused on using PV area diagnostics to quantify dynamical variability. Both diabatic heating and divergence associated with monsoon deep convection increases low PV areas at levels above the convection (Figure 2). Model results (Appendix A) show that the convective forcing of the anticyclone can be well represented by the divergence integrated over the area of low PV. The divergence provides a useful, concise diagnostic of the forcing of low PV area (i.e., anticyclone strength), with significantly higher correlations than OLR.

[33] The temporal variability in the anticyclone strength is closely linked to variability in the convective forcing. The main period of variability in low PV areas of 30–40 days

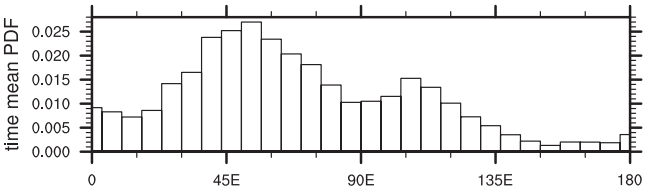

Figure 15. Probability distribution function of low PV area (PV $\leq$1.6 PVU) at 380 K for May–September 2006 (as in Figure 6, top panel).

can be explained by forcing from the divergence term, which is linked to variability in convection. Convection associated with the Asian monsoon is subject to intraseasonal variability with periods around both 10–20 and 30–90 days [*Annamalai and Slingo*, 2001], often referred to as dry and wet spells or active and break periods (for an overview, see *Lau et al.* [2012]). Our results demonstrate that the intraseasonal variability in the surface monsoon system with periods around 30–40 days is reflected in the upper tropospheric circulation. The forcing of low PV by convection occurs mostly over longitudes 70°E–110°E. From there, low PV is often advected to the west and occasionally to the east. The eastward propagation of low PV air might furthermore interact with Rossby wave breaking events that often occur in this region [*Postel and Hitchman*, 1999]. The more frequent westward propagation, often appearing following periods of strong convective forcing, may be related to advection in the anticyclonic easterly winds, and/or some contribution from dynamical instabilities (eddy shedding) as suggested by *Hsu and Plumb* [2000]. Because the anticyclone is forced by strongly transient convection (contrasting the steadily forced calculations of *Hsu and Plumb* [2000]), it is difficult to identify the relative roles of variable forcing versus intrinsic instability in the system. Thus, the overall picture of the anticyclone in terms of PV is forcing by convection at its center followed by PV eddy transport and subsequent mixing, possibly associated with instabilities, that decays the anticyclone strength. This finding is in agreement with *Plumb* [2007] in that PV eddy transport balances the convective forcing of the anticyclone.

[34] The bimodality in the location of the anticyclone found in earlier studies [*Zhang et al.*, 2002] in 100 hPa geopotential height is not reflected in the 360 K (i.e., about 150 hPa) low PV area investigated here (see Figure 6, top panel). At 380 K, which is closer to 100 hPa as used in *Zhang et al.* [2002], the probability distribution of low PV air shows two maxima, one at around 50°E and one around 105°E (see Figure 15). However, low PV area at 380 K as diagnostic for the anticyclone strength suffers from the following deficit: Over the summer season, mean PV in the monsoon region increases. Consequently, PV values below a certain threshold occur only at the beginning of the season. As noted in section 5, this leads to low correlations of PV area at 380 K with the occurrence of high CO concentrations. The causes for the increase of mean PV over the monsoon season are not entirely clear, although it could be related to a steady rise of the 380 K level over the season. The topics of how the monsoon PV dynamics at higher altitudes relate to the variability at 360 K, and whether the bimodality might be a feature observed only at higher altitudes, we leave to future studies.

[35] The use of PV area as diagnostic was motivated in parts by earlier studies of the stratospheric polar vortex. While the polar vortex and the anticyclone have very different forcing mechanisms (slow seasonal variation in diabatic cooling versus highly variable deep convection), both are large-scale systems with strong winds that act as transport barriers. However, while the polar vortex forms strong transport barriers at its edge, reflected in strong PV gradients, the anticyclone only shows strong PV gradients toward the extratropics. PV gradients within the anticyclone and toward the (sub)tropics are weak, indicative of strong mixing, likely associated with eddy shedding.

[36] The spatial variability of the anticyclone in terms of PV is reflected in chemical tracer fields, as shown here for CO observed by the MLS instrument. Enhanced CO is well correlated with the spatial distribution of low PV, and transient eddy shedding events observed for low PV air are generally also found to carry air with elevated CO concentrations (Figures 10 and 11). Thus, tracers that are transported through the Asian monsoon to the upper troposphere could be efficiently mixed in this region. Remapping CO in anticyclone equivalent latitude shows that highest CO concentrations are generally found in the center of the anticyclone, i.e., where PV is lowest. Relatively high CO concentrations are typically confined to the area of low PV, and seasonal variations in the extent of the anticyclone are matched by the extension of the region of elevated CO concentrations. Time variations in the amount of CO within the anticyclone are less well correlated with the strength of the anticyclone. A simple explanation for this is that the upward transport of CO from the surface to the upper troposphere is not only controlled by the strength of deep convection (which drives the anticyclone) but also by the source distribution of CO at the surface. Not only is the emission of CO variable in time and space but also for CO to be transported into the upper troposphere convective inflow needs be located at a region of high surface concentrations. If, for example, strong convection occurs over CO-poor areas, the convection will result in an increase of the anticyclone strength but not increase the CO concentrations. At higher altitudes, at the upper part of the anticyclone (around 380 K), we find enhanced CO concentrations are better correlated with the anticyclone strength (Figure 15). The modeling study of *Park et al.* [2009] suggested that CO transport to levels around 100 hPa is determined by vertical advection (as part of the three-dimensional monsoon circulation), while convective transport is dominant at lower altitudes. If the strength of the vertical advection is coupled to the strength of the anticyclone as measured by low PV areas at 360 K, then stronger temporal coupling to CO at 380 K may be expected. Furthermore, the confinement of air within the anticyclone might change with height, which could further affect the covariability of the strength of the anticyclone and tracer anomalies.

Appendix A: Anticyclone PV Budget in a Free-Running GCM Simulation

[37] Because of the complexity of diagnosing the PV budget for the monsoon anticyclone based on reanalysis

data (with uncertainties in diabatic heating and divergence estimates, in addition to tendencies from assimilation increments), we have performed PV budget calculations using a free-running chemistry-climate model (CCM) simulation. The CCM used here is the Whole Atmosphere Community Climate Model WACCM [*Garcia et al.*, 2007].

[38] The overall behavior and variability of the Asian anticyclone in WACCM is similar to observations. The budget of the area of low PV (≤0.3 PVU) calculated over the region of 15°N–45°N and 0°E–180°E is shown for one May–September season in Figure A1. The model data are of lower horizontal (1.9° latitude × 2.5° longitude) and temporal (daily) resolution compared to MERRA. This lower resolution leads to an overall smoother time series of low PV areas and their drivers compared to the full-resolution MERRA data. However, the MERRA results are comparable to the model if the MERRA data are sampled at similar resolution.

[39] The PV tendency budget (Figure A1b) shows that the diabatic and divergence terms are positive, of similar size and well correlated in the model, and these two terms lead to increases in low PV area linked to enhanced convection. The actual area changes (tendency term) are small compared to the forcing terms, and the forcing is balanced by a strong negative term, calculated here as residual (Figure A1b, green line). The residual represents the mixing term in equation (3), which by definition cannot be calculated explicitly as it involves subscale mixing. Equating the calculated residual to (unresolved) damping or PV mixing, we interpret the balance in Figure A1 as follows.

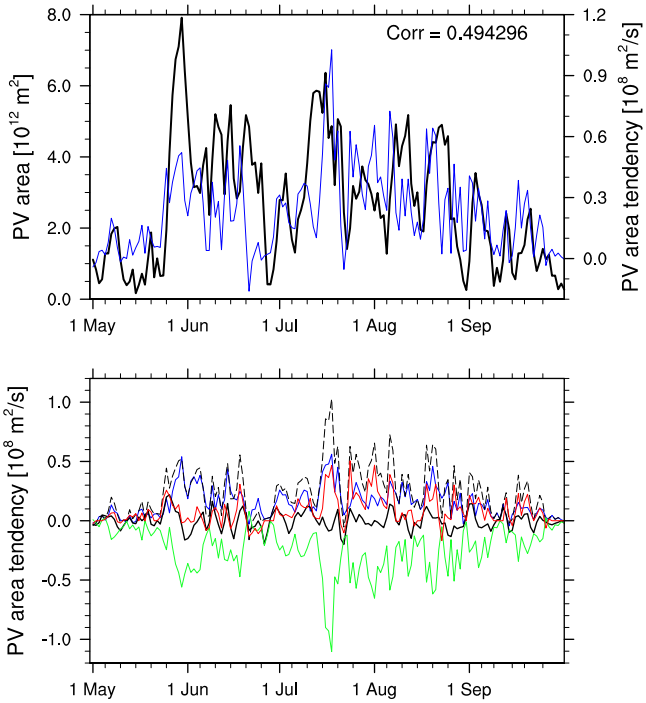

Figure A1. Budget of 0.3 PV area for one season from WACCM. (top) Area of PV = 0.3 PVU (black) and forcing term (blue, divergence + diabatic term). (bottom) PV area tendency (black) with divergence term (blue), diabatic term (red), sum of diabatic and divergence terms (dashed black), and residual (green).

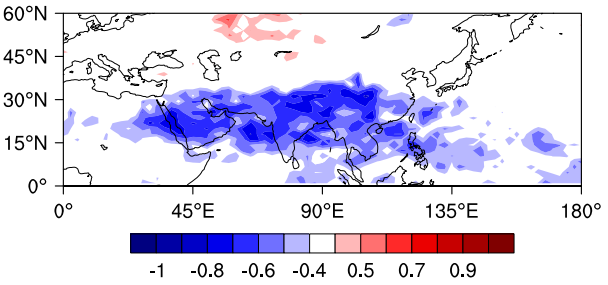

Figure A2. Correlation of divergence and the vertical gradient of diabatic heating calculated from one season (May–September) from WACCM.

The primary PV balance is between forcing (diabatic and divergence terms) and damping, with the calculated area tendency a small difference. Empirically, both the forcing and damping terms are strongly correlated with the PV area (Figure A1a). Furthermore, the diabatic and divergence terms are well correlated in the model (Figure A2), as can be expected from the relation of the vertical gradient of diabatic heating to divergence through the continuity equation. Thus, the overall forcing can be approximated as proportional to the divergence term alone. These model results are consistent with the strong correlations between the PV area and divergence forcing as derived from MERRA data in section 4.2. The divergence appears to be a useful proxy for the dynamical effects of convection in forcing PV anomalies within the anticyclone.

[40] **Acknowledgments.** HG was funded under a postdoc scholarship by the Deutsche Akademische Austauschdienst (DAAD). We thank D. Kinnison for providing WACCM data, and M. Park, L. Pan, and C. Homeyer for discussion and helpful comments on the manuscript.

References

Annamalai, H., and J. M. Slingo (2001), Active/break cycles: Diagnosis of the intraseasonal variability of the Asian summer monsoon, *Clim. Dyn.*, *18*, 85–102, doi:10.1007/s003820100161.

Baker, A. K., T. J. Schuck, F. Slemr, P. van Velthoven, A. Zahn, and C. A. M. Brenninkmeijer (2011), Characterization of non-methane hydrocarbons in Asian summer monsoon outflow observed by the caribic aircraft, *Atmos. Chem. Phys.*, *11*, 503–518, doi:10.5194/acp-11-503-2011.

Bodeker, G., J. Scott, K. Kreher, and R. McKenzie (2001), Global ozone trends in potential vorticity coordinates using toms and gome intercompared against the Dobson network: 1978–1998, *J. Geophys. Res.*, *106*(D19), 23,029–23,042.

Butchart, N., and E. Remsberg (1986), The area of the stratospheric polar vortex as a diagnostic for tracer transport on an isentropic surface, *J. Atmos. Sci.*, *43*(13), 1319–1339.

Dethof, A., A. O'Neill, J. M. Slingo, and H. G. J. Smit (1999), A mechanism for moistening the lower stratosphere involving the Asian summer monsoon, *Q. J. R. Meteorol. Soc.*, *125*, 1079–1106.

Garcia, R. R., D. R. Marsh, D. E. Kinnison, B. A. Boville, and F. Sassi (2007), Simulation of secular trends in the middle atmosphere, 1950–2003, *J. Geophys. Res.*, *112*, D09301, doi:10.1029/2006JD007485.

Gill, A. E. (1980), Some simple solutions for heat-induced tropical circulation, *Q. J. R. Meteorol. Soc.*, *106*, 447–462, doi:10.1256/smsqj.44904.

Haynes, P. H., and M. E. McIntyre (1987), On the evolution of vorticity and potential vorticity in the presence of diabatic heating and frictional or other forces, *J. Atmos. Sci.*, *44*, 828–841, doi:10.1175/1520-0469(1987)044.

Holton, J. R. (2004), *An Introduction to Dynamic Meteorology*, 4th ed., International Geophysics Series, Academic Press, San Diego, New York.

Hoskins, B. J., and M. J. Rodwell (1995), A model of the Asian summer monsoon, I: The global scale, *J. Atmos. Sci.*, *52*, 1329–1340.

Hsu, C., and R. Plumb (2000), Non-axisymmetric thermally driven circulations and upper tropospheric monsoon dynamics, *J. Atmos. Sci.*, *57*, 1254–1276.

Lau, W. K.-M., D. E. Waliser, and B. N. Goswami (2012), *South Asian Monsoon*, pp. 21–72, Springer Praxis Books, Springer, Berlin Heidelberg.

Liebmann, B., and C. Smith (1996), Description of a complete (interpolated) outgoing longwave radiation dataset, *Bull. Am. Meteorol. Soc.*, *77*, 1275–1277.

Livesey, N. J., et al. (2011), Version 3.3 level 2 data quality and description document, *Tech. Rep.*, Jet Propul. Lab., Pasadena, Calif.

Manney, G. L., M. J. Schwartz, K. Krüger, M. L. Santee, S. Pawson, J. N. Lee, W. H. Daffer, R. A. Fuller, and N. J. Livesey (2009), Aura microwave limb sounder observations of dynamics and transport during the record-breaking 2009 Arctic stratospheric major warming, *Geophys. Res. Lett.*, *36*, L12815, doi:10.1029/2009GL038586.

Nash, E. R., P. A. Newman, J. E. Rosenfield, and M. R. Schoeberl (1996), An objective determination of the polar vortex using Ertel's potential vorticity, *J. Geophys. Res.*, *101*, 9471–9478.

Park, M., W. J. Randel, A. Gettelman, S. T. Massie, and J. H. Jiang (2007), Transport above the Asian summer monsoon anticyclone inferred from aura microwave limb sounder tracers, *J. Geophys. Res.*, *112*, D16309, doi:10.1029/2006JD008294.

Park, M., W. J. Randel, L. K. Emmons, P. F. Bernath, K. A. Walker, and C. D. Boone (2008), Chemical isolation in the Asian monsoon anticyclone observed in Atmospheric Chemistry Experiment (ACE-FTS) data, *Atmos. Chem. Phys.*, *8*, 757–764.

Park, M., W. J. Randel, L. K. Emmons, and N. J. Livesey (2009), Transport pathways of carbon monoxide in the Asian summer monsoon diagnosed from model of ozone and related tracers (MOZART), *J. Geophys. Res.*, *114*, D08303, doi:10.1029/2008JD010621.

Plumb, R. A. (2007), Dynamical constraints on monsoon circulations. *The Global Circulation of the Atmosphere*, pp. 252–266, Princeton Univ. Press, Princeton.

Popovic, J. M., and R. A. Plumb (2001), Eddy shedding from the upper tropospheric Asian monsoon anticyclone, *J. Atmos. Sci.*, *58*, 93–104.

Postel, G. A., and M. H. Hitchman (1999), A climatology of Rossby wave breaking along the subtropical tropopause, *J. Atmos. Sci.*, *56*, 359–373, doi:10.1175/1520-0469(1999)056<0359:ACORWB.

Randel, W. J., and M. Park (2006), Deep convective influence on the Asian summer monsoon anticyclone and associated tracer variability observed with atmospheric infrared sounder (AIRS), *J. Geophys. Res.*, *111*, D12314, doi:10.1029/2005JD006490.

Rienecker, M. M., et al. (2011), MERRA: NASA's Modern-Era Retrospective Analysis for Research and Applications, *J. Clim.*, *24*, 3624–3648.

Santee, M., G. Manney, N. Livesey, L. Froidevaux, M. Schwartz, and W. Read (2011), Trace gas evolution in the lowermost stratosphere from aura microwave limb sounder measurements, *J. Geophys. Res.*, *116*, D18306, doi:10.1029/2011JD015590.

Sardeshmukh, P. D., and I. M. Held (1984), The vorticity balance in the tropical upper troposphere of a general circulation model, *J. Atmos. Sci.*, *41*, 768–778, doi:10.1175/1520-0469(1984)041<0768:TVBIT.

Waugh, D. W., and P.-P. Rong (2002), Interannual variability in the decay of lower stratospheric Arctic vortices, *J. Meteorol. Soc. Jpn.*, *80*(4B), 997–1012.

Yan, R.-C., J.-C. Bian, and Q.-J. Fan (2011), The impact of the South Asia high bimodality on the chemical composition of the upper troposphere and lower stratosphere, *Atmos. Oceanic Sci. Lett.*, *4*, 229–234.

Zhang, Q., G. Wu, and Y. Qian (2002), The bimodality of the 100 hpa South Asia high and its relationship to the climate anomaly over East Asia in summer, *J. Meteorol. Soc. Jpn.*, *80*(4), 733–744.